

# CFD predictions of NREL Phase VI Rotor Experiments in NASA/AMES Wind tunnel

Mukesh M. Yelmule\*<sup>‡</sup>, EswaraRao Anjuri VSJ\*

\*Engineering Competence Center, Assistant Lead Engineer, Vestas Technology R&D Chennai Pvt. Ltd.

yemuk@vestas.com, esran@vestas.com

<sup>‡</sup>Corresponding Author; Mukesh M. Yelmule, Vestas Technology R&D Chennai Pvt. Ltd. Block A, 8th Floor, TECCI Park, 173, Rajiv Gandhi Salai, Sholinganallur, Chennai-600119, India., +91 9600012903, yemuk@vestas.com

*Received: 17.01.2013 Accepted: 13.02.2013*

**Abstract-** This article presents the computational predictions of NREL Phase VI rotor, a stall-regulated two bladed wind turbine with full-span pitch control and a power rating of 20 kW, in the NASA/AMES 80 ft. X 120 ft. wind tunnel. A 3D CFD-RANS approach is used, modeling single blade of the rotor utilizing periodicity, in a rotating frame of reference; over several upwind cases. All the simulations are performed using the commercial multi-purpose CFD solver ANSYS CFX 12.1. The blade is modeled with simplified spherical hub excluding nacelle and tower, at stationary wind conditions neglecting wall shear effects due to tunnel blockage. The comparisons are done for the blade with 0° yaw angle and 3° tip pitch angle. Reasonably good agreement is obtained when comparing modeled mechanical effects Viz. power, thrust, and span wise force components with measurements over wind speeds ranging from 5m/s to 25m/s. The capability of CFD in predicting complex 3D wind turbine aerodynamics is demonstrated in this paper with NREL Phase VI data campaign as a case study.

**Keywords-** NREL-VI Rotor, Navier–Stokes equations, Computational fluid dynamics, Wind turbine aerodynamics, Simulation.

## 1. Introduction

Accurate aerodynamic predictions are required in the design of new rotor blades and additional passive/active performance improvement devices. This requires continued validation of new and existing design tools & methods, increased accuracy and efficiency of the results. CFD is one such design tool & extensive research has been done in developing the CFD tools and methods for predicting aerodynamics of wind turbines during the last few years.

During the last decade, CFD modeling of wind turbines has evolved from scientific work performed at research institutions and investigations performed at wind turbine manufacturers with the application of commercial codes. Traditionally the wind turbine blades are designed using first principles (BEM theory) utilizing 2D airfoil tables from wind tunnel. Empirical corrections are used to account for 3D effects Viz. tip losses, root losses, rotational effects, and dynamic stall effects. High fidelity CFD naturally includes these phenomena, but has more difficulty in modeling and other wind turbine phenomena such as variable turbulent

inflow and boundary layer transition [7]. CFD has been used to improve the aerodynamic design of wind turbines including tip shapes, winglets and hub modeling [8, 9, 10, and 11] where it captures flow physics better at which BEM models are no longer applicable. High fidelity Navier-Stokes based computational fluid dynamics is currently making inroads into many phases of industrial wind energy design [1, 2]. CFD is used for the analysis of both 2D airfoils and also 3D blades [1, 2, 3, 4, and 5].

The NREL Phase VI Unsteady Aerodynamic Experiment [1, 2, and 18] provides an excellent validation test case for 3D CFD Rotor analyses. The Phase VI test campaign performed in the NASA Ames National Full-Scale Aerodynamic Complex (NFAC) was completed in the year 2000. The 2-bladed, 10.058m diameter, stall regulated turbine has a power rating of 20kW. The blades are twisted and mildly tapered. Multidisciplinary measurements were obtained over a wide range of operating conditions. Experimental measurements included blade pressures and resulting integrated air loads, shaft torque, sectional inflow conditions, blade root strain, tip acceleration and wake

visualization. Both upwind and downwind configurations with rigid and teetering blades were run for speeds from 5 m/s to 25 m/s. Yawed and unsteady pitch configurations are also available. Free and fixed transition results were measured. The blade uses specially designed S809 airfoil for which experimental aerodynamic performance parameters are available. Blade structural properties are well documented [21]. Various researchers [3, 12, 13, 14, 15, 16, 17, 18, 19, and 20] have investigated this configuration numerically using a range of CFD methods and grid topologies.

Researchers at Risø computed the isolated rotor with and without wind tunnel walls using a multi-block, structured mesh, incompressible solver EllipSys3D with a RANS turbulence model [18] and a detached eddy simulation [19]. Performance was generally well captured although stall initiation at 10 m/s wind speed was missed.

The objective of the present work is to validate the CFD method utilizing commercial multi-purpose CFD solver ANSYS CFX 12.1 & Multi block structured mesh generator ICFM-CFD, with the NREL Phase VI rotor (Test sequence S) wind turbine experiments. This report mainly consists of

- CFD Modeling of the NREL Phase VI rotor
- Comparison of integrated quantities
- Flow visualization
- Comparison of span-wise sectional details
- Comparison of 2D airfoil characteristics
- Comparison with other CFD predictions
- Conclusions

## 2. CFD Modelling of NREL Phase VI Rotor

In the present work a compressible Navier-Stokes solver (CFX) is utilized to predict the aerodynamics of the Phase VI rotor from the National Renewable Energy Laboratory. The two-bladed 10.058m diameter rotor geometry is based on the S809 airfoil. The details about the blade & measurement conventions can be found in [21]. The rotor cone angle is 0° and the tip pitch angle is set to 3°. In this investigation, only Sequence S upwind configuration is examined, and the operational conditions for the cases computed can be found in Table 1.

**Table 1.** Sequence S Operating conditions.

Test Data Series S			
Wind m/sec	Rot Speed RPM	Density kg/m <sup>3</sup>	Pitch-B1 deg
5.038456	71.685051	1.243452	2.988024
7.016254	71.866684	1.245786	2.988288
10.047129	72.096161	1.24589	2.988288
13.069461	72.094017	1.226576	2.979884
15.098236	72.061897	1.224037	2.98147
20.130888	72.008751	1.221355	2.985683
25.108795	72.162216	1.219688	2.988288

In the current work, a single blade is modeled in CFD considering the periodic boundary conditions that is

equivalent to 180° periodic sector of the rotor, to save computational resource. Only the wind speed, RPM and density are used as input variables for CFD simulations without any empirical tuning of the existing models.

ANSYS CFX 12.1 uses a finite-volume based unstructured parallelized coupled algebraic multi-grid solver with a second order advection scheme and second order overall accuracy [22]. The computations have been performed with compressible Reynolds Averaged Navier-Stokes (RANS) equations and the SST [23] turbulence model. The transition from laminar to turbulent flow is modeled using Langtry and Menter correlation based Gamma-Theta transition model. The default correlations in the model are proprietary of ANSYS and therefore not known in detail by the user. In general the default correlation for  $Re_{\text{ot}}$  is based on the free stream turbulence intensity and the pressure gradient outside the boundary layer. The value of  $Re_{\text{ot}}$  determined outside of the boundary layer is diffused into the boundary layer by a standard diffusion term. The physics of the transition process is not directly modeled by the two additional transport equations. Instead, the physics of the transition process is entirely contained in the underlying experimental correlations.

As the turbine is upwind type, exclusion of tower in the CFD model has negligible effect on rotor aerodynamics & is a sound choice. The theoretical definition of the S809 airfoil has a very sharp trailing edge; whereas the geometry used for CFD simulations has trailing edge thickness of 1mm along the entire span of blade that resembles the actual blade used for experimentation. Rotor computations are stationary, at constant uniform wind speed, constant pitch and RPM neglecting the unsteady inflow, which is a fair choice considering that the experimental data set is arrived statistically from a large number of repeated measurements.

Uniform velocity normal to the inlet is used at inlet boundary and atmospheric static pressure is used at outlet and far-field boundaries. Blade and hub surfaces are defined as no-slip walls with specified rotation. Figure 1 shows different boundaries and the blade.

Figure 2 shows the mesh on different boundaries including the blade. All computations are run in parallel on the computing cluster.

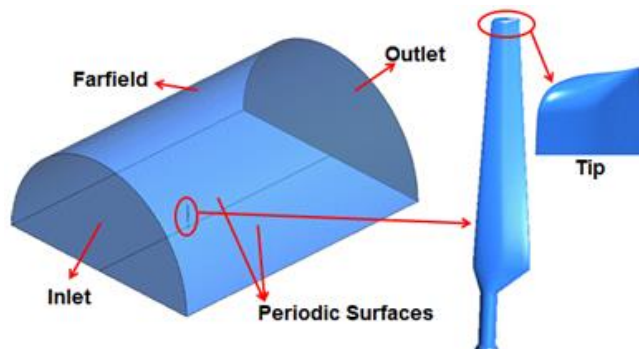


**Fig. 1.** Computational domain, boundaries and blade.

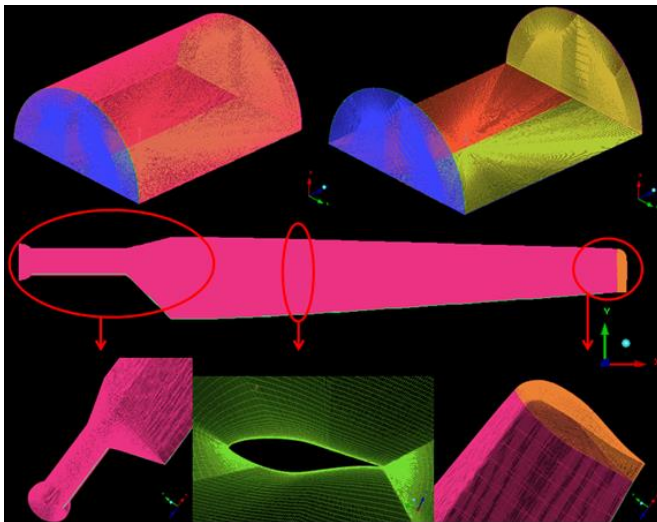


Fig. 2. Computational mesh on boundaries and blade.

The steady state simulations are performed for approximately 900 iterations ensuring convergence (residuals  $\leq 10e-4$  & imbalances  $< 1\%$ ). It took approximately 24 hours of computing time with 32 CPU's.

### 3. Comparison of Integrated Quantities

Mechanical Power (P) is calculated by monitoring the torque T about the flow axis and multiplying with the angular velocity  $\Omega$  (as shown in equation 1).

$$P = T\Omega \tag{1}$$

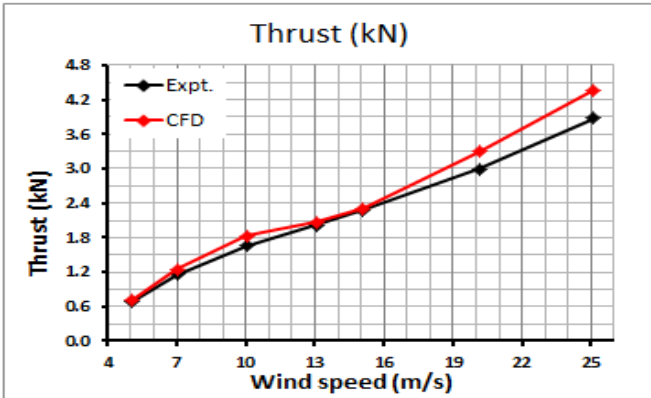
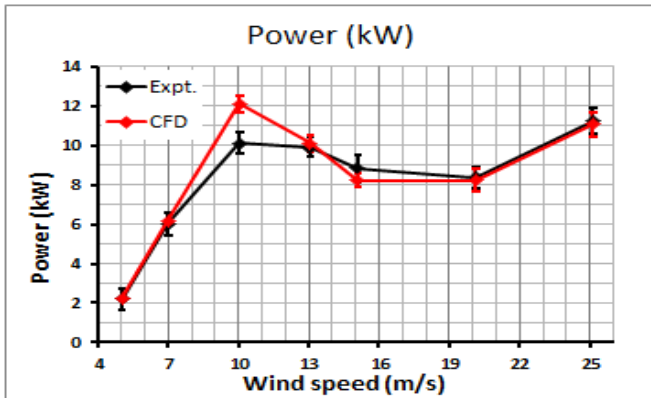


Fig. 3. Comparison of measured and CFD Integrated quantities.

It is observed from Fig.3 that integrated quantities Viz. Power & Thrust, from CFD compare well with experimental results at all wind velocities, except at 10 m/s, where an over-prediction up to 20 % is observed.

### 4. Flow Visualisations

Figure 4 shows surface streamlines and Fig.5 shows turbulence intermittency contours on the suction side of blade indicating transition at 7 m/s, 10 m/s and 20 m/s wind speed. The vertical lines show span-wise sections Viz. 30%, 46.7%, 63.3%, 80%, 95%, where pressure measurements are available .It is observed that at low wind speed up to 7 m/s, the flow is attached except up to 30 % span & the transition line is clearly visible. At 10 m/s the flow is separated over the entire span except close to 95 % span, where transition can be clearly seen , and close to mid-span (47.7% span) the separation line has moved to the leading edge. At 20 m/s the separation has spread over the entire blade and the flow is fully turbulent across the span.

### 5. Comparison of Span-Wise Sectional Details

From the experiment pressure measurements are available at five span-wise sections Viz. 30 %, 46.7%, 63.3%, 80%, 95% r/R. The stagnation point dynamic pressure is used to non-dimensionalise the pressure.

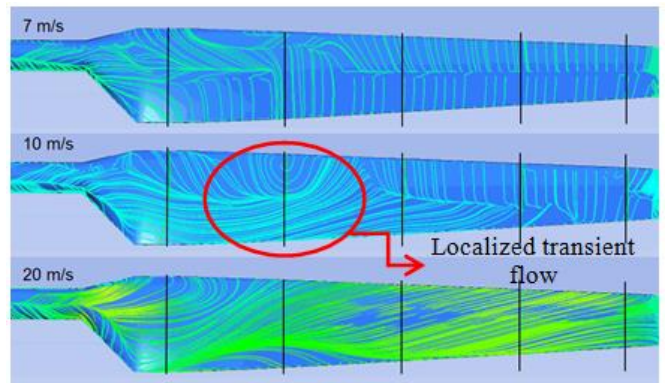


Fig. 4. Surface streamlines at 7 m/s, 10 m/s & 20 m/s wind speed.

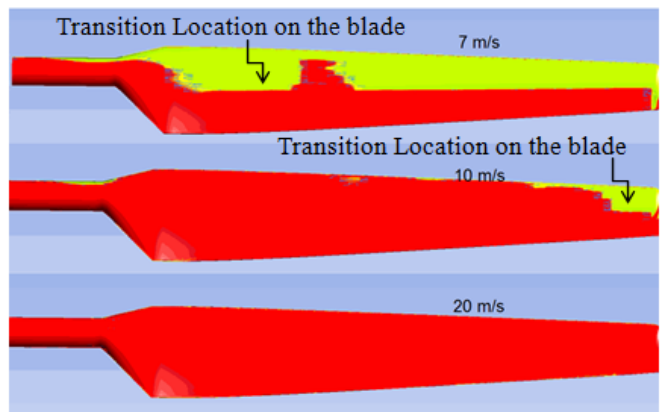


Fig. 5. Turbulence intermittency on suction side of the blade at 7m/s, 10 m/s & 20 m/s wind speed.

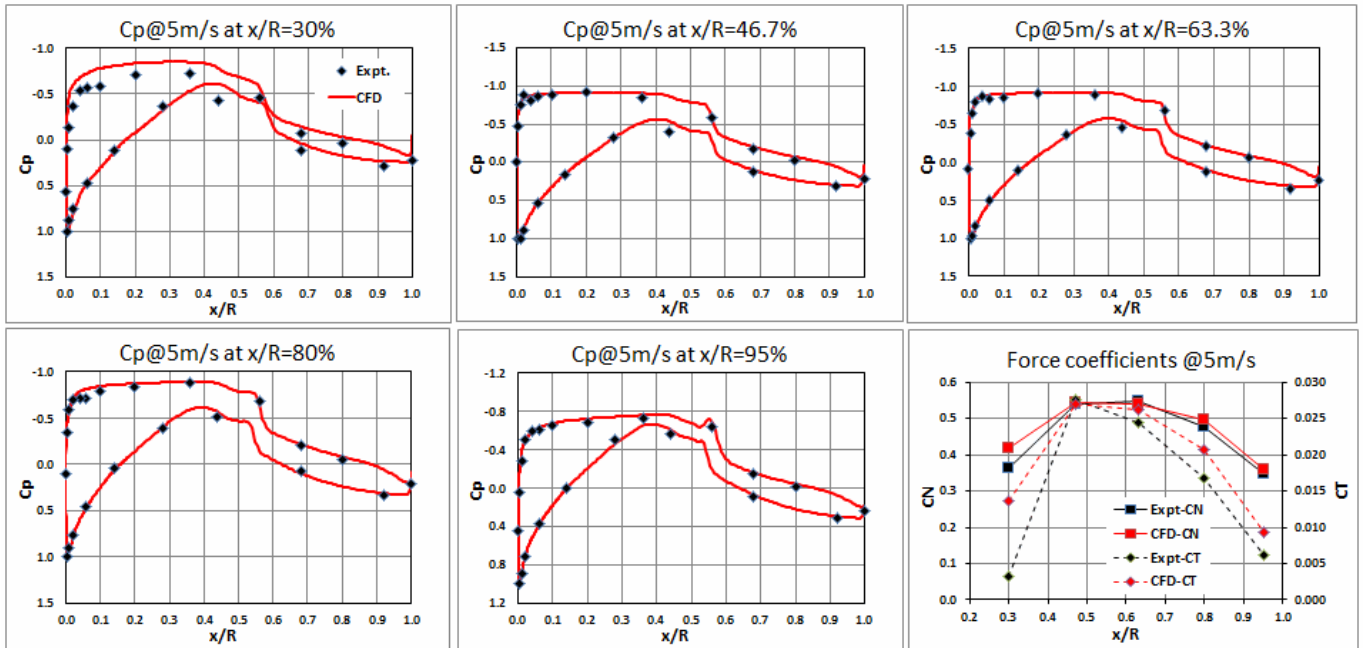


Fig. 6. Comparison of CFD and measured pressure distributions at 5m/s wind speed.

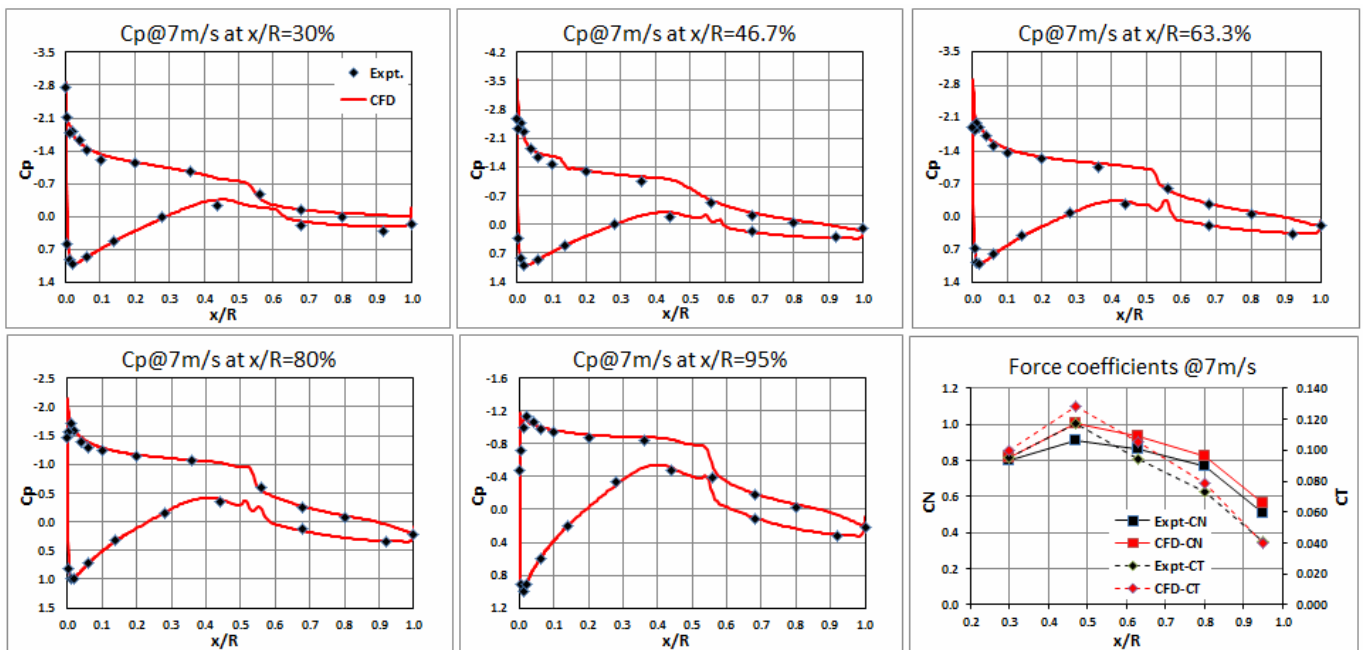


Fig. 7. Comparison of CFD and measured pressure distributions at 7m/s wind speed.

Figure 6 and Fig. 7 show pressure distribution at 5m/s and 7m/s wind speed, which is categorized as low wind speed region. Referring Fig. 4 to Fig. 7, the flow is mostly attached and is in good agreement with the measured pressure distribution except up to 30% span, where flow is separated and we observe some deviation that is due to a known difficulty of RANS turbulence models in solving separated flow.

Figure 8 shows pressure distribution & force coefficients at 10 m/s wind speed which is categorized as onset of stall. A discrepancy in pressure near the leading edge of suction surface (Peak suction pressure) is observed at 46.7 % span

due to flow separation close to mid-span and resulting localized transient stall effects making the peak suction pressure practically difficult to capture in the experiments. The same can be observed from sudden dip of tangential force coefficient CT at 46.7% span.

Figure 9 & Fig. 10 show pressure distribution and force coefficients at 13 m/s & 15 m/s respectively, which are categorized as stall region, where the flow is separated over the entire blade except close to the tip. The separation that started at mid span for 10 m/s wind speed moves progressively towards the outer span of blade with increase in wind speed, the same is observed from widening of CT

dip. Figure 11 & Fig.12 show pressure distribution and force coefficients at 20 m/s & 25 m/s respectively, which are categorized as deep stall region, where the flow is separated over entire span and the blade is completely stalled. Deviation is observed in the suction side pressure distribution in stall and deep stall region, due to difficulty of RANS models in solving separated flows. This difference however does not cause substantial differences to integrated quantities, which is a characteristic specific to S809 airfoil at higher angle of attack and is in agreement with observations from [18].

Although quantitative differences exist in the normal & tangential force coefficients between computed and

experimental data, the trends agree well for all the wind velocities. The fact that the number of pressure probes placed along the airfoil to reconstruct the pressure distribution from experiments has a physical limitation compared to no limitations in CFD simulations reflects in deviations. For e.g. in experiment data at 22 pressure probes is available along the airfoil, while CFD simulations have 700 grid/data points along the airfoil. Thus CN, CT calculated with experimental pressure distribution assumes linear pressure variation between any two consecutive measurements, whereas CFD has a much finely resolved pressure profile.

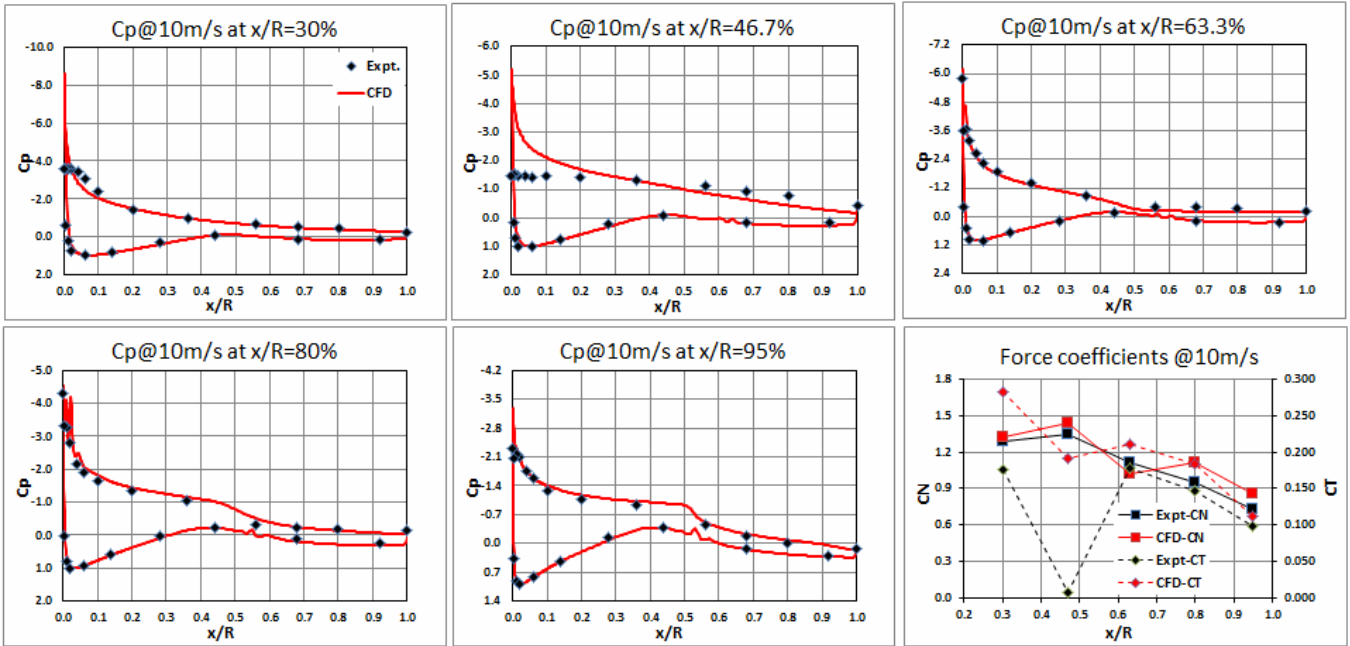


Fig. 8. Comparison of CFD and measured pressure distributions at 10m/s wind speed.

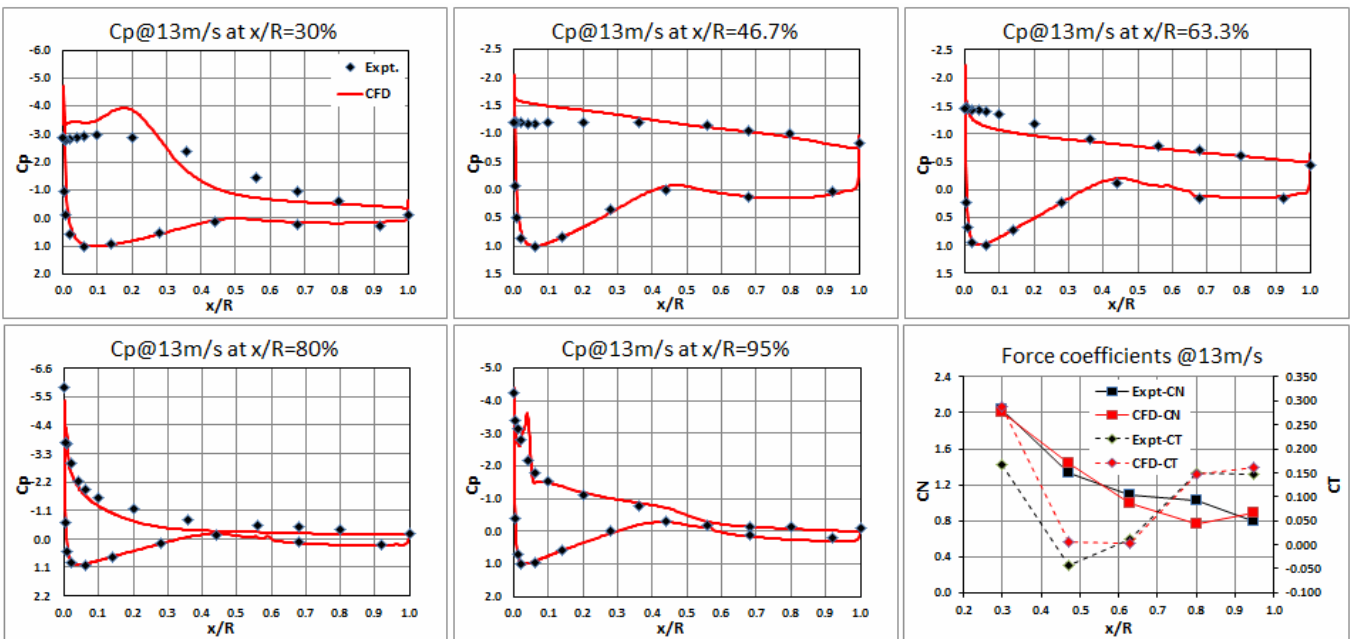


Fig. 9. Comparison of CFD and measured pressure distributions at 13m/s wind speed.

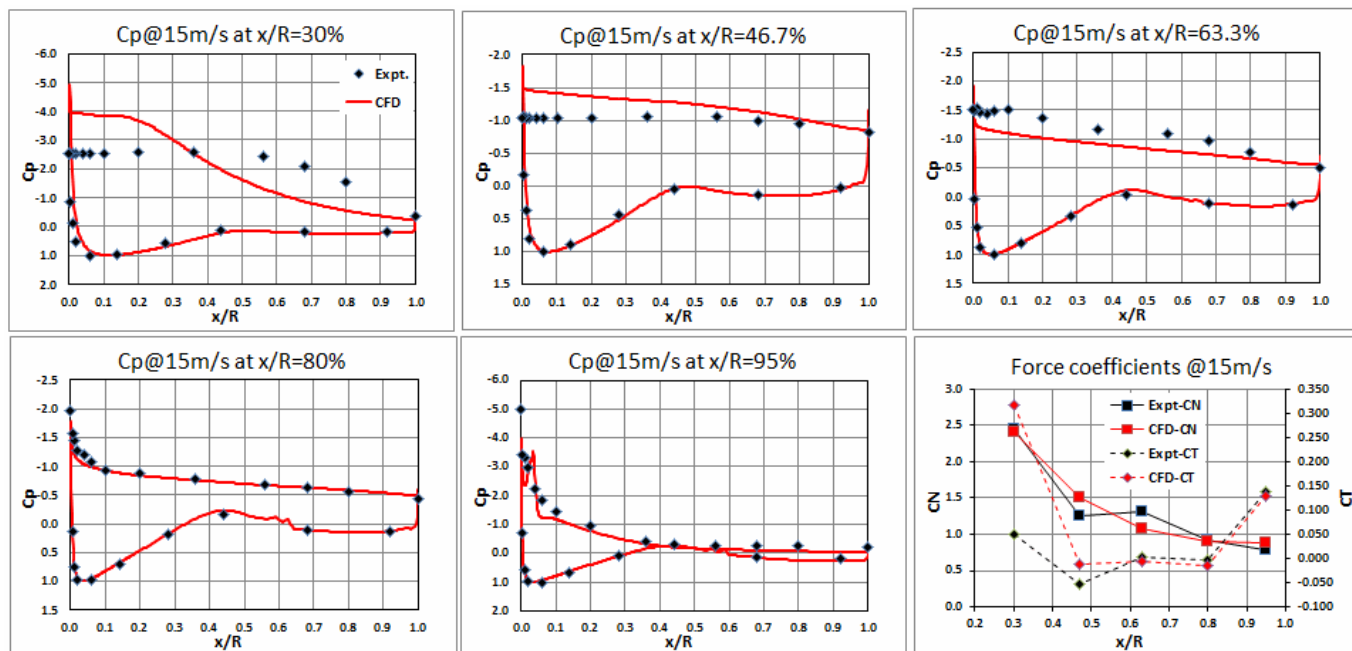


Fig. 10. Comparison of CFD and measured pressure distributions at 15m/s wind speed.

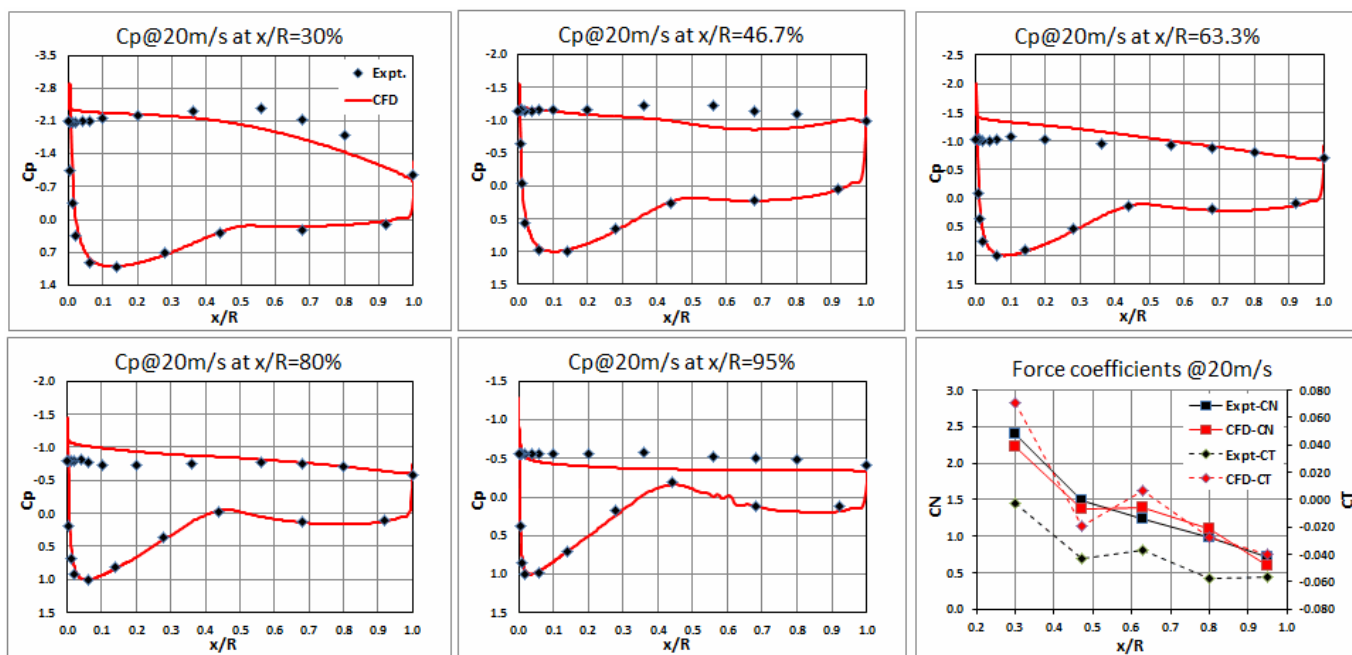


Fig. 11. Comparison of CFD and measured pressure distributions at 20m/s wind speed.

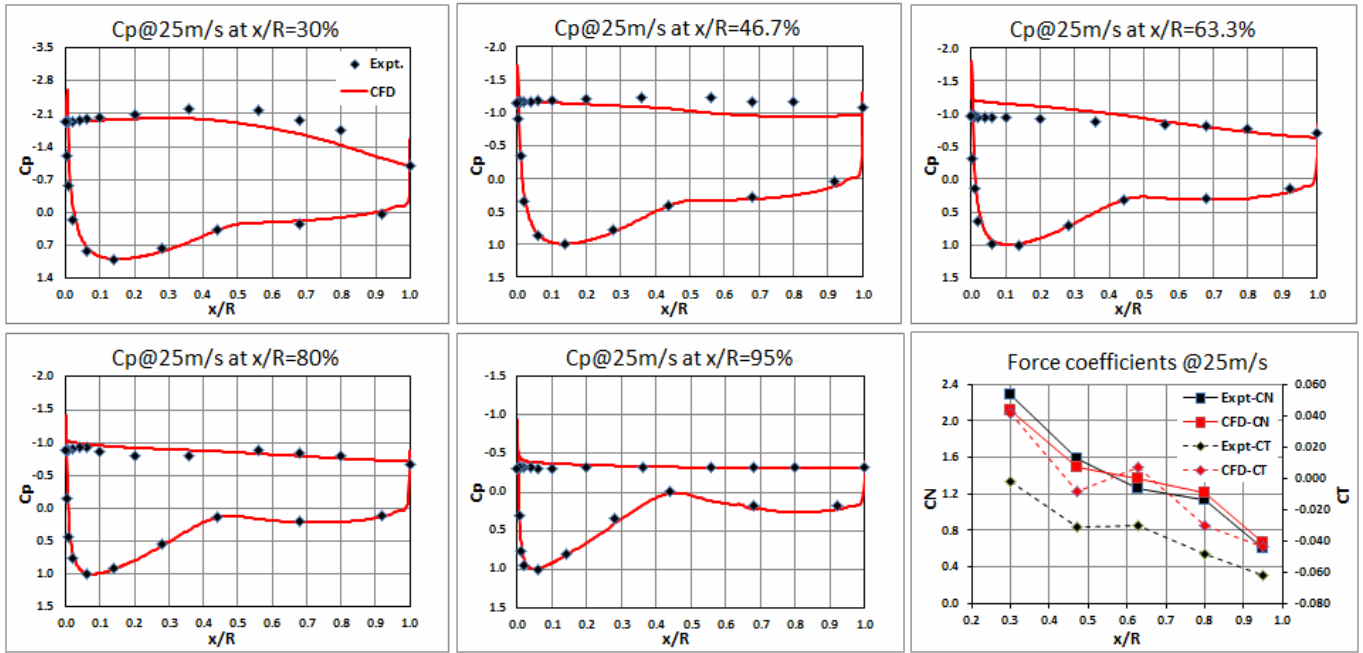


Fig. 12. Comparison of CFD and measured pressure distributions at 25m/s wind speed.

6. Comparison of 2D Airfoil Characteristics

Figure 13 shows the 2d characteristics extracted from 3D CFD at 5 span-wise locations Viz. 29%, 48%, 66%, 79% & 93% using the method described in [25].

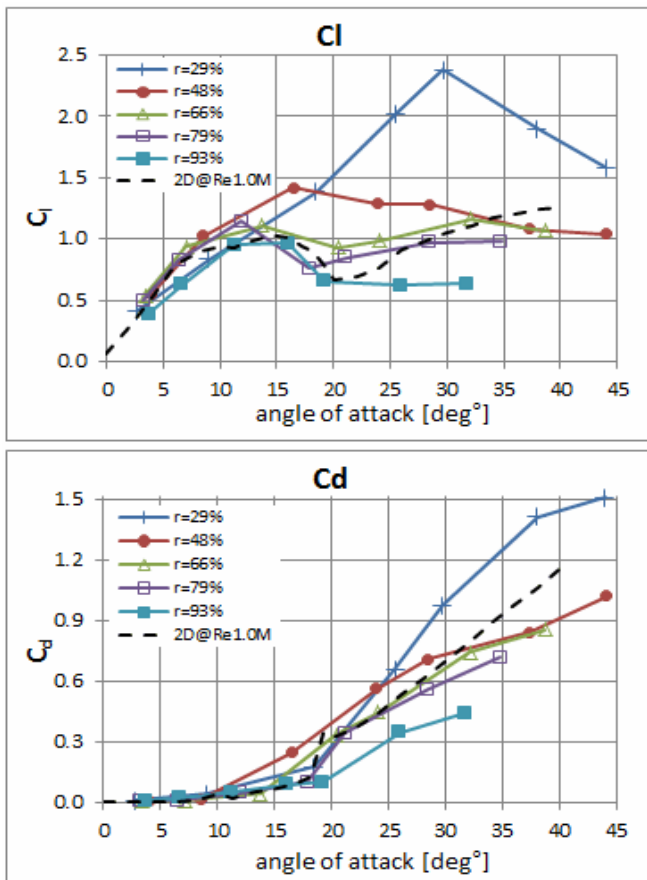


Fig. 13. 2D characteristics extracted from 3D CFD

It is compared with 2D OSU WT (wind tunnel) data of S809 airfoil with natural transition. It is observed that the lift is comparatively higher in the inboard section for high angle of attack that is in good agreement with theoretical himmelskamp effect. It is also observed that the drag is comparatively higher, thus the higher lift in inboard sections is at the cost of higher drag. For the outer span-wise locations Viz. 66% and 79 % span Cl & Cd compare well with WT data , these locations thus are least affected by inboard and outboard radial flow. At 93 % span the tip effects influence the flow and lowers Cl & Cd that again is in good qualitative agreement with theory.

7. Comparison with Other CFD Predictions

Figure 14 shows the comparison of our CFD results (CFX) with other CFD predictions Viz. BEM, Risoe (Ellipsys 3D) & GRI (Acusolve) for NREL Phase VI rotor test sequence S. Note that the Risoe (Ellipsys 3D) predictions are for fully turbulent flow conditions.

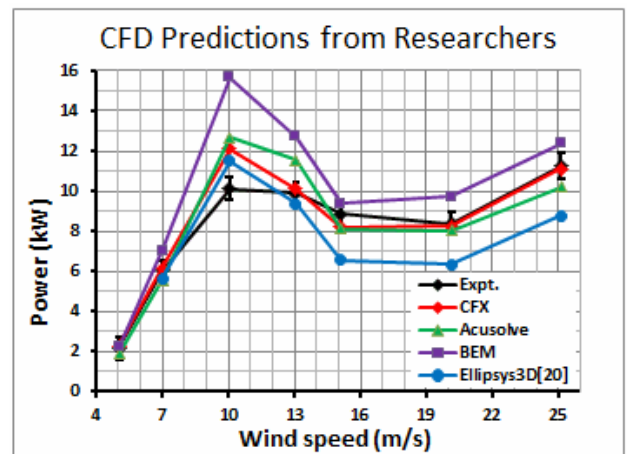


Fig. 14. Comparison of CFD results with other researchers

A good comparison is observed for CFX predictions with experiments and other CFD researchers.

## 8. Conclusion

Computational fluid dynamics calculations have been executed for NREL Phase VI rotor at upwind conditions with 0° yaw and 3° tip pitch. A single blade has been analyzed with 180° periodicity and structured mesh using commercial multi-purpose CFD solver ANSYS CFX 12.1. The steady state CFD data is compared with the measured wind tunnel data. CFD rotor computations show good qualitative and quantitative comparison with measurements except at the onset of stall (10 m/s).

At low wind speed (5 m/s & 7 m/s) flow is attached except up to 30 % span and transition occurs close to mid-chord. CFD predictions are accurate & within the measurement range.

At the onset of stall (10 m/s) separation occurs close to mid span at leading edge. Steady state CFD fails to predict the power and thrust within measurement range and is well known for its difficulty in capturing highly transient effects at the onset of stall. This reflects in over-prediction as high as 20 % in power.

In stall (13 m/s and 15 m/s) and deep stall (20 m/s & 25 m/s), the separation that initiated at mid-span (at 10 m/s) progressively moves over the entire span with increase in wind speed. Steady state CFD predicts integrated quantities within measurement range, although quantitative differences are observed in pressure distribution on suction side, due to the specific stall behavior of S809 airfoil.

Additionally flow visualization and comparison of 2D airfoil characteristics extracted from 3D CFD with OSU WT airfoil data gives more insight and understanding of complex 3D effects making CFD computations more competitive & generic compared to design methods based on 2D theoretical models that rely on empirical tuning & corrections.

## Acknowledgements

We acknowledge Vestas Technology R&D Chennai Private Limited, ECC (Engineering Competence Centre), Simulation competence for the technical and computational resources availed during these CFD computations. We are also grateful to Vestas Americas, GRI (Global Research and Innovation) for collaborating with NREL & making authentic NREL data available for comparison.

## References

[1] Larsen, J., "ANSYS CFD Applied to Wind Turbines at Siemens Wind Power," ANSYS Conference & 26th CADFEM Users' Meeting, Darmstadt, Germany, October 2008.  
[2] Standish, K., "CFD at GE", Wind Power 2007, Los Angeles, CA, June 2007.

[3] Le Pape, A., and Gleize, V., "Improved Navier-Stokes Computations of a Stall-Regulated Wind Turbine Using Low Mach Number Preconditioning," 44th AIAA Aerospace Sciences Meeting and Exhibit, Reno, NV, January 2006, AIAA 2006-1502.  
[4] Standish, K. J., and van Dam, C. P., "Aerodynamic Analysis of Blunt Trailing Edge Airfoils," Journal of Solar Energy Engineering, Vol. 125, No. 4, Nov. 2003, pp. 479-487.  
[5] Fuglsang, P., and Bak, C., "Development of the Risø Wind Turbine Airfoils," Wind Energy, Vol. 7, No. 2, May 2004, p. 145-162.  
[6] Xu, G. and Sankar, L., "Development of Engineering Aerodynamics Models Using a Viscous Flow methodology on the NREL Phase VI Rotor", Wind Energy, vol. 5, no. 2-3, pp. 171-183, 2002.  
[7] Langtry, R. B, Gola, J, and Menter, F. R, "Predicting 2D Airfoil and 3D Wind Turbine Rotor Performance using a Transition Model for General CFD Codes," 44th AIAA Aerospace Sciences Meeting and Exhibit, Reno, NV, January 2006, AIAA-2006-395.  
[8] Johansen J., Madsen, H. A., Sørensen, N. N., and Bak C., "Numerical Investigation of a Wind Turbine Rotor with an Aerodynamically Redesigned Hub-Region," 2006 European Wind Energy Conference and Exhibition, Athens, Greece, 2006.  
[9] Johansen J., and Sørensen N. N.: "Aerodynamic investigation of winglets on wind turbine blades using CFD", Risø-R- 1543(EN) report 2006.  
[10] Hansen, M. O. L., and Johansen, J., "Tip Studies Using CFD and Comparison with Tip Loss Models," Wind Energy, 2004, p. 343 -356.  
[11] Hjort, S., Laursen, J., and Enevoldsen, P., "Aerodynamic Winglet Optimization," Sandia National Lab Blade Workshop, May 2008.  
[12] Duque, E. P. N., Burkland, M. D., and Johnson, W., "Navier-Stokes and comprehensive analysis performance predictions of the NREL phase VI experiment," Journal of Solar Energy Engineering 2003; 125: 457-467.  
[13] Chao, D. D., and van Dam, C. P., "Computational Aerodynamic Analysis of a Blunt Trailing-edge Airfoil Modification to the NREL Phase VI Rotor," Wind Energy, July 2007, 10:529-550.  
[14] Gonzalez A., and Munduate, X., "Three-dimensional and Rotational Aerodynamics on the NREL Phase VI Wind Turbine Blade," 45th AIAA Aerospace Sciences Meeting and Exhibit, Reno, NV, January 2007, AIAA 2007-0628.  
[15] Schmitz, S., and Chattot, J-J., "Application of a 'Parallelized Coupled Navier-Stokes/Vortex Panel Solver' to the NREL Phase VI Rotor," 43rd AIAA Aerospace Sciences Meeting and Exhibit, Reno, NV, January 2003, AIAA 2003-0593.

- [16] Zahle, F., Johansen, J., Sorenson, N., and Graham, J., "Wind Turbine Rotor-Tower Interaction Using an Incompressible Overset Grid Method," AIAA 45th Aerospace Sciences Meeting and Exhibit, Reno, NV, January 2007, AIAA 2007-0425.
- [17] Simms, D. A., Schreck, S., Hand, M., and Fingersh, L., J., "NREL Unsteady Aerodynamics Experiment in the NASA Ames Wind Tunnel: A Comparison of Predictions to Measurements" NREL/TP-500-29494, June 2001.
- [18] Sørensen, N. N., Michelsen, J. A., and Schreck, S., "Navier-Stokes Predictions of the NREL Phase VI rotor in the NASA Ames 80ft x120 ft wind tunnel," Wind Energy, Vol. 5, No. 2-3, 2002, pp. 151-169.
- [19] Johansen, J., Sørensen, N. N., Michelsen, J. A., and Schreck, S., "Detached-Eddy Simulation of Flow around the NREL Phase-VI Rotor," Wind Energy, Vol. 5, No. 2-3, 2002, pp. 185-197.
- [20] Mark A. Potsdam, Dimitri J. Mavriplis, "Unstructured Mesh CFD Aerodynamic Analysis of the NREL Phase VI Rotor", AIAA 2009-1221, 47th AIAA Aerospace Sciences Meeting Including The New Horizons Forum and Aerospace Exposition, 5 - 8 January 2009, Orlando, Florida.
- [21] M.M. Hand, D.A. Simms, L.J. Fingersh, D.W. Jager, J.R. Cotrell, S. Schreck, and S.M. Larwood, "Unsteady Aerodynamics Experiment Phase VI: Wind Tunnel Test Configurations and Available Data Campaigns", NREL/TP-500-29955, December 2001.
- [22] Technical information regarding the ANSYS-CFX solver: <http://www.ansys.com/products/cfxadvanced-solver.asp>.
- [23] Menter FR. Two-equation eddy-viscosity model for engineering applications. AIAA-Journal 1994; 32(8):1598-1605.
- [24] Robin Langtry, Florian Menter, "Overview of Industrial Transition Modeling in CFX", ANSYS Germany GmbH, ANSYS CFX.
- [25] Jeppe Johansen and Niels N. Sørensen, "Aerofoil Characteristics from 3D CFD Rotor Computations", Risø National Laboratory, PO Box 49, DK-4000 Roskilde, Denmark.